JOURNAL OF THERMOPHYSICS AND HEAT TRANSFER
Vol. 8, No. 4, Oct.–Dec. 1994

Simulation of Heat and Momentum Transfer in Complex Microgeometries

Ali Beskok* and George E. Karniadakis†
Brown University, Providence, Rhode Island 02912

In this article we present a time-accurate computational model based on the slip-flow theory to simulate momentum and heat transport phenomena in complex microgeometries, encountered in typical components of microdevices such as microcapillaries, microvalves, microrotors, and microbearings. In the first part, we present extensions to the classical Maxwell/Smoluchowski slip conditions to include high-order Knudsen number effects as well as to take into account the coupling of momentum and heat transfer through thermal creep and viscous heating effects. The numerical method is based on the spectral element technique; validation of the method is obtained by comparison of the numerical simulation results in simple prototype flows (e.g., channel slip-flows) with analytical results. Reduction of pressure drop in microchannels, reported in similar experimental studies, is investigated using slip-flow theory and simulations. In the second part, we consider model inlet flows and a slip-flow past a microcylinder. The effect of slip-flow on skin friction reduction and associated increase in mass flow rate as well as the variation of normal stresses is investigated as a function of Knudsen number. Finally, the effect of compressibility is examined and possible extensions of the current model to take into account such effect are discussed.

I. Introduction

THERE has been great interest in the applications of microdynamical devices over the last 5 yr in such diverse areas as instrumentation, microelectronics, bioengineering, and advanced energy microsystems.[1,2] In the beginning, the emphasis was in developing efficient fabrication techniques for microdevices. However, with the successful design and fabrication of a variety of such devices the interest is shifting towards developing techniques in efficiently predicting their functionality, i.e., transient response, structural integrity, transport processes, etc. Computational modeling and simulation can provide such a predictive capability and means of evaluating the performance of a new design before hardware fabrication. The numerical simulation of the dynamical phenomena in the microdomain, however, should be based on the principal governing laws in microscales for which there is currently a lack of fundamental understanding.

In particular, momentum and heat transport phenomena in the basic components of microdevices such as microcapillaries, microvalves, and microbearings are not well understood. Since the seminal work of Eringen on microfluids,[3] no significant progress has been made to derive general constitutive equations based on a microscopic approach. Therefore, in considering the process of momentum exchange and heat transfer by convection of a gas with a solid surface in microdomains (e.g., with characteristic length varying from 100 to 0.1 μm), both the macroscopic or continuum model, as well as the molecular or microscopic model, should be considered. The distinction among the various regimes and corresponding describing models can be obtained with the introduction of the Knudsen number Kn, which is defined as $Kn = (\lambda/L)$, where λ is the mean free path of the molecules, and L is a characteristic flow dimension. The characteristic length is typically proportional to domain length; however, it should be chosen so that it accommodates all length scales including gradients of density, velocity, pressure, and temperature within the flow.

In the continuum limit, values of parameters at different points in the domain essentially represent averages of the microscopic behavior in the neighborhood of the point. This assumption eventually leads to the formulation of the Navier-Stokes and energy equations as being the governing equations. However, these continuum equations that express conservation of mass, momentum, and energy, break down for finite values of the Knudsen number. For the aforementioned range of characteristic lengths and for a typical value of mean free path for air $\lambda \approx 10^{-7}$ m, the corresponding Knudsen number varies from 0.001 to 1. In the lower Knudsen limit the deviation of molecular motion from a standard Maxwellian distribution is still sufficiently small, and the Navier-Stokes equations modified appropriately (e.g., using the Chapman-Enskog theory for the transport coefficients) govern the flow.[4] On the other hand, in the higher Knudsen number limit the only closed equation that is strictly applicable is the Boltzmann equation that involves the molecular velocities as the dependent parameters instead of the macroscopic quantities.

In the case of a rarefied gas flow the following empirical information is available.[5] For $Kn \leq 10^{-3}$ the fluid can be considered as a continuum, while for $Kn \geq 10$ it is considered a free molecular flow. A rarefied gas can neither be considered an absolutely continuous medium nor a free-molecule flow at Knudsen number between 10^{-3}–10. In that region, a further classification is needed[5]: slip-flow ($10^{-3} < Kn < 0.1$) and transition flow ($0.1 < Kn < 10$). In the region of slip and early transition flow, velocity and temperature distributions in the flowfield can still be determined from the Navier-Stokes and the energy equation if velocity-slip and temperature-jump at the walls are taken into account via the slip boundary conditions. This approach has been followed in the past in hypersonic flow as an alternative to modeling rarefied gas effects through modification of the stress tensor.[6] In the most general case, these boundary conditions (usually referred

Received Aug. 12, 1993; revision received Feb. 18, 1994; accepted for publication Feb. 22. 1994.

*Student in Absentia at Princeton University, Princeton, NJ 08540; currently at Division of Applied Mathematics, Center for Fluid Mechanics. Student Member AIAA.

†Associate Professor, Division of Applied Mathematics, Center for Fluid Mechanics.

to as the Maxwell/Smoluchowski slip conditions) are given in[5]

$$u_{\text{gas}} - u_{\text{wall}} = \frac{2 - \sigma_v}{\sigma_v} \frac{1}{\rho(2RT_w/\pi)^{1/2}} \tau_s + \frac{3}{4} \frac{Pr(\gamma - 1)}{\gamma \rho R T_w} (-q_s) \tag{1a}$$

$$T_{\text{gas}} - T_{\text{wall}} = \frac{2 - \sigma_T}{\sigma_T} \left[\frac{2(\gamma - 1)}{\gamma + 1} \right] \frac{1}{R\rho(2RT_w/\pi)^{1/2}} (-q_n) \tag{1b}$$

where q_n, q_s are the normal and tangential heat transfer components in the gas, and τ_s is the viscous stress component corresponding to the skin friction, R is the gas constant, γ is the ratio of specific heats, ρ is the density, u_w and T_w are the wall velocity and temperature, respectively, and Pr is the Prandtl number. The term in the above equation proportional to $(-q_s)$ is associated with the phenomena of thermal creep, which can be important in causing variation of pressure along tubes in the presence of tangential temperature gradient. The coefficients σ_v and σ_T are the tangential momentum and energy accommodation coefficients, respectively. These coefficients reflect the nature of momentum and energy transfer between the impinging gas molecules and the surface. For example, $\sigma_v = 0.0$ corresponds to specular reflection, and $\sigma_v = 1.0$ corresponds to diffuse reflection. In the first case, the tangential velocity of the molecules reflected from the walls is unchanged and the normal velocity of the molecules is reversed due to the normal momentum transfer to the wall. In the second case, the molecules are reflected from the walls with zero average tangential velocity. The diffuse reflection, in particular, is an important phenomenon for tangential momentum exchange (and thus friction) of the gas with the walls. In the equation above, slip is assumed even for the diffuse reflection case. Therefore, the no-slip condition on the walls is obtained only when $Kn = 0.0$. The accommodation coefficients depend on the gas and surface temperatures, local pressure, and possibly the velocity and the mean direction of the local flow, and they are tabulated for some common gases and surfaces[7]; under laboratory conditions values as low as 0.2 have been observed.[8] Very low values of σ_v will increase the slip on the walls considerably even for small Knudsen number flows. For microflows surface roughness may play an important role in momentum and energy transport; its effects can be implicitly included in the model via the accommodation coefficients.

In the present study we consider the slip-flow regime and formulate a numerical algorithm appropriate for simulations of time-dependent slip-flows in complex microgeometries. The numerical scheme is based on the spectral element method we have developed for simulation of flows in macroscales[9,10]; it provides high-order accuracy and flexibility in discretizing geometries of arbitrary complexity. These features eliminate numerical artifacts and are prerequisite for a successful "standalone" simulation approach required in studies of transport phenomena in microdomains. We also modify the slip-flow boundary condition [Eq. (1)] to include nonlinear (high-order) effects. With this formulation we consider simulations of slip-flow in prototype geometries including internal flows, e.g., channel microflows as well as external flows, e.g., slip-flow past a circular microcylinder. Validation of the simulation results is obtained using analytical and semi-empirical solutions of rarefied gas dynamics,[11-13] as well as preliminary comparisons with available experimental data.[14]

This article is organized as follows. In Sec. II, we present the formulation for the slip-flow regime and develop the new velocity-slip boundary condition. In Sec. III, we present analytical results and numerical simulation examples of microflows in internal and external flows. Finally, we summarize our results in Sec. IV and discuss the limitations of the current formulation and numerical methodology.

II. Modeling and Formulation

The governing equations for the slip-flow regime are the Navier-Stokes and energy equations. For computational convenience, we consider here the incompressible form of the equations given in nondimensional form as follows:

$$\frac{D\boldsymbol{u}}{Dt} = -\frac{\nabla p}{\rho} + Re^{-1}\nabla^2 \boldsymbol{u} \quad \text{in} \quad \Omega \tag{2a}$$

$$\frac{DT}{Dt} = Pr^{-1}Re^{-1}\nabla^2 T + EcRe^{-1}\frac{1}{2}\left(\frac{\partial u_i}{\partial x_j} + \frac{\partial u_j}{\partial x_i}\right)^2 \quad \text{in} \quad \Omega \tag{2b}$$

$$\nabla \cdot \boldsymbol{u} = 0 \quad \text{in} \quad \Omega \tag{2c}$$

where $\boldsymbol{u}$ is the velocity field $\boldsymbol{u}(\boldsymbol{x}, t)$, p is the static pressure, $T(\boldsymbol{x}, t)$ is the temperature, and ρ is the density. Here, Re, Pr, and Ec are the Reynolds, Prandtl, and Eckert numbers, respectively; D denotes total derivative, and Ω represents the flow domain. We assume that the fluid properties are constant and that no high-order corrections are needed in the equations of motion for $Kn \leq 0.1$.[4]

The velocity-slip and temperature-jump boundary conditions can be obtained by an approximate analysis of the motion of a monatomic gas near an isothermal surface. The derivation of velocity slip formula given in Ref. 5 considers first-order slip effects. The uncoupled velocity-slip and temperature-jump boundary conditions [Eq. (1)], rewritten here in nondimensional form are

$$u_{\text{gas}} - u_{\text{wall}} = \frac{2 - \sigma_v}{\sigma_v} Kn \frac{\partial u_s}{\partial n} \tag{3a}$$

$$T_{\text{gas}} - T_{\text{wall}} = \frac{2 - \sigma_T}{\sigma_T} \left[\frac{2\gamma}{\gamma + 1} \right] \frac{Kn}{Pr} \frac{\partial T}{\partial n} \tag{3b}$$

where $(\partial u_s/\partial n)$ and $(\partial T/\partial n)$ shows the variation of tangential velocity and temperature normal to the surface.

The first-order slip-flow boundary conditions given in Eqs. (3a) and (3b) do not include the thermal creep effects, which vary quadratically with Kn. It is possible to obtain higher-order corrections to the above velocity-slip boundary condition by retaining higher order terms in the Taylor series expansion of tangential velocity near the vicinity of walls. To this end, we consider an approximate analysis of the motion of a monatomic gas near an isothermal surface. Very close to the wall, it can be asssumed that half of the molecules are coming from the layer of gas, one mean free path λ away, while the other half of the molecules are reflected from the wall. Furthermore, we assume that $(1 - \sigma_v)$ of the molecules are reflected from the wall "specularly," and σ_v of the molecules are assumed to be reflected "diffusively" from the wall with average tangential velocity that of the wall. Following Ref. 5, with normal coordinate to the wall denoted as n and replacing λ with Kn in nondimensional form we obtain:

$$U_s = \frac{1}{2}\left[U_s + Kn\left(\frac{\partial U}{\partial n}\right)_s + \frac{Kn^2}{2}\left(\frac{\partial^2 U}{\partial n^2}\right)_s + \cdots \right] + \frac{1}{2}\left\{ (1 - \sigma_v)\left[U_s + Kn\left(\frac{\partial U}{\partial n}\right)_s + \frac{Kn^2}{2}\left(\frac{\partial^2 U}{\partial n^2}\right)_s + \cdots \right] + \sigma \cdot U_w \right\} \tag{4}$$

where the subscript s shows near-wall conditions. This expansion results in the following slip relation on the boundaries:

$$U_s - U_w = \frac{2 - \sigma_v}{\sigma_v}\left[Kn\left(\frac{\partial U}{\partial n}\right)_s + \frac{Kn^2}{2}\left(\frac{\partial^2 U}{\partial n^2}\right)_s + \cdots\right] \quad (5)$$

We can also write an asymptotic expansion of the velocity field in terms of Kn, i.e.,

$$U = U_0 + KnU_1 + Kn^2U_2 + Kn^3U_3 + \mathcal{O}(Kn^4) \quad (6)$$

where the no-slip velocity field is denoted by $U_0(x, t)$, and corrections due to the different orders of Kn are denoted as $U_i(x, t)$, $(i = 1, 2, 3, \ldots)$. Our objective is to establish a methodology to develop slip boundary conditions accurate up to the second-order terms in Kn. Let us first introduce a new slip boundary condition in a general form

$$U_s - U_w = \frac{2 - \sigma}{\sigma}\frac{Kn}{1 - B(Kn)Kn}\frac{\partial U}{\partial n} \quad (7)$$

where $B(Kn)$ is a parameter to be determined. For a general choice of $B(Kn)$, Eq. (7) is first-order accurate in Kn. However, there are two specific values of $B(Kn)$ corresponding to the continuum ($Kn \to 0$) and the free molecular ($Kn \to \infty$) flow regimes. The value of $B(Kn)$ as $Kn \to 0.0$ is used to make Eq. (7) second-order accurate in Kn for finite but small values of Kn. Equation (7) suggests finite corrections for slip effects provided that $B(Kn) \leq 0$. It is possible to determine the value of $B(Kn)$ for small Kn corresponding to the slip-flow regime by Taylor series expansion of $B(Kn)$ about $Kn = 0$, i.e.,

$$B(Kn) = B|_0 + \left.\frac{dB}{dKn}\right|_0 Kn + \cdots = b + Knc + \cdots \quad (8)$$

Assuming that $BKn < 1$, we can expand Eq. (7) with a geometric series incorporating Eq. (8) for $B(Kn)$. This results in

$$U_s - U_w = \frac{2 - \sigma}{\sigma} Kn \frac{\partial U}{\partial n}[1 + bKn + (b^2 + c)Kn^2 + \cdots] \quad (9)$$

A high-order slip boundary condition is obtained by substituting the asymptotic expansion for the velocity field [Eq. (6)] into the geometric series expansion given in Eq. (9). Comparing the resulting equations with Eq. (5), and matching the second-order terms, we determine the unknown b as[15]

$$b = (U_0''/2U_0')|_s \quad (10)$$

The quantities U_0' and U_0'' denote first and second derivatives of tangential component of velocity vector along the normal direction to the surface and corresponds to a continuum (no-slip) solution. Uncertainties in the accommodation coefficients may mask the second-order corrections for small Kn flows. However, uncertainties associated with the measurement of these values can be absorbed into the variable $B(Kn)$ in the general form of the high-order slip boundary condition, see Eq. (7). High-order temperature jump boundary conditions could be derived for the energy equation similarly. Higher-order boundary conditions in the context of the Burnett equations are reviewed in Ref. 16, and a second-order boundary condition for the lubrication equation is derived in Ref. 17. Our boundary condition requires the computation of higher-order derivatives only of the continuum field, and thus it is easier to be implemented.

The high-order slip boundary conditions including thermal creep effects are therefore

$$u_{gas} - u_{wall} = \frac{2 - \sigma_v}{\sigma_v}\frac{Kn}{1 - bKn}\frac{\partial u_s}{\partial n} + \frac{3}{2\pi}\frac{(\gamma - 1)}{\gamma}\frac{Kn^2Re}{Ec}\frac{\partial T}{\partial s} \quad (11a)$$

$$T_{gas} - T_{wall} = \frac{2 - \sigma_T}{\sigma_T}\left(\frac{2\gamma}{\gamma + 1}\right)\frac{Kn}{Pr}\frac{\partial T}{\partial n} \quad (11b)$$

where $(\partial T/\partial s)$ is the tangential temperature variation along the channel surface.

To fully determine momentum and energy transport in microgeometries we need the following nondimensional numbers: the Reynolds, Prandtl, Eckert, and Knudsen numbers. However, it is possible to introduce a functional relation for Knudsen number, and Eckert number in terms of Mach number, i.e., $M = (U/\sqrt{\gamma RT_0})$. The Knudsen number can be written in terms of Mach number, and Reynolds number as

$$Kn = (\sqrt{\pi\gamma/2}M/Re) \quad (12)$$

while the Eckert number can be written as

$$Ec = (\gamma - 1)(T_0/\Delta T)M^2 \quad (13)$$

where ΔT is the specified temperature difference in the domain, and T_0 is the reference temperature used to define the Mach number. Using the functional relations for Ec and Kn, the independent parameters of the problem are reduced to three (Pr, Re, and M).

The incompressiblity assumption stated in Eq. (2c) restricts application of our results to flows with small temperature and pressure fluctuations compared to the reference pressure and temperature. For this reason, the specified temperature difference in the domain ΔT and the reference Mach number of the flows are kept small in this study (i.e., $\Delta T \sim \mathcal{O}(1)$ and $M \leq 0.2$).

In general, Eq. (2) is coupled since a velocity-slip along a solid surface is always accompanied with a temperature-jump. This coupled set of equations along with the most general boundary conditions described in Eqs. (11a) and (11b) are solved using the spectral element method.[9,10,15] In the spectral element discretization, the computational domain is broken up into K macroelements, and the dependent and independent variables are approximated by Nth-order tensor-product polynomial expansions within the individual elements. Variational/quadrature operators are used to generate the discrete equations with interfacial continuity constraints imposed naturally via the variational statement. The temporal discretization is obtained using the recently developed high-order time splitting algorithm, which employs stiffly stable time integration rules in three successive substeps that treat the convective, pressure, and viscous terms in the equations of motion.[18]

III. Simulation of Prototype Flows

A. Internal Flows

In this section, a detailed analysis of momentum and heat transport for a pressure-driven microchannel flow is presented. The effects of thermal creep on transport processes is also investigated. Our analysis assumes a steady, fully developed flow subject to a specified heat flux.

The momentum Eq. (2a) subject to slip boundary conditions with a specified tangential temperature variation [see Eq. (11a)] can be solved analytically.[15] The noncontinuum effects on momentum transfer can be investigated by either analyzing the increase of volumetric flow rate of the channel under a constant pressure difference, or by analyzing the change

in the drag of the channel for fixed volumetric flow rate under appropriately specified pressure gradient. The nondimensional velocity distribution in a channel extending from $y = -1$ to $y = 1$ is

$$U(y) = \frac{Re}{2}\left|\frac{\partial p}{\partial x}\right|\left[1 - y^2 + 2\left(\frac{2-\sigma_v}{\sigma_v}\right)\frac{Kn}{1+\frac{1}{2}Kn}\right] + \frac{3}{2\pi}\frac{(\gamma-1)}{\gamma}\frac{Kn^2 Re}{Ec}\frac{\partial T_s}{\partial x} \tag{14}$$

where $(\partial T_s/\partial x)$ denotes the tangential temperature variation along the channel surface. Given this parabolic velocity profile we obtain the coefficient of high-order boundary condition from Eq. (10) to be $b = -\frac{1}{2}$. Correspondingly, the volumetric flow rate $\dot{Q}$ through the channel becomes, in nondimensional form $[|(\partial P/\partial x)| = (2/Re)]$

$$\dot{Q} = \frac{4}{3} + 4\left(\frac{2-\sigma_v}{\sigma_v}\right)\frac{Kn}{1+\frac{1}{2}Kn} + \frac{3}{\pi}\frac{(\gamma-1)}{\gamma}\frac{Kn^2 Re}{Ec}\frac{\partial T_s}{\partial x} \tag{15}$$

The leading-order variations in the volumetric flow rate under fixed $(\partial p/\partial x)$ is linear in Kn due to velocity slip, and quadratic in Kn due to thermal creep effects.

An interesting feature of noncontinuum flows is the possibility of starting the flow with creep effects rather than a specified pressure gradient. In that case, the flow starts creeping along the channel surface and finally interacts with the stagnant fluid layers. This creates shear stresses, which result in turning on the velocity slip mechanism.[19] It is also possible to maintain zero average flow rate in a channel under a prescribed pressure gradient, if the pressure gradient and the thermal creep effects balance each other. For an incompressible flow, this condition can be maintained if

$$\frac{\partial p}{\partial x} = \frac{\frac{9}{2\pi}\frac{(\gamma-1)}{\gamma}Kn^2\frac{\partial T_s}{\partial x}}{Ec\left[1 + 3\left(\frac{2-\sigma_v}{\sigma_v}\right)\frac{Kn}{1+\frac{1}{2}Kn}\right]} \tag{16}$$

In this case [if $(\partial T_s/\partial x) > 0$], the flow creeps from cold to hot direction along the channel surface, where a positive pressure gradient creates backflow in the middle of the channel. In regards to the effects of thermal creep on drag coefficient of the flow for a fixed volumetric flow rate, the ratio of the drag coefficient of a slip surface C_D to the drag coefficient C_{D_0} of a no-slip surface is given by

$$\frac{C_D}{C_{D_0}} = \frac{1 - \frac{3}{\pi\dot{Q}}Kn^2\frac{Re}{Ec}\frac{\partial T_s}{\partial x}}{1 + 3\frac{2-\sigma_v}{\sigma_v}\left(\frac{Kn}{1+\frac{1}{2}Kn}\right)} \tag{17}$$

where $C_D = (\tau_s/0.5\rho U^2)Re$. It is seen that for fixed $\dot{Q}$, Ec, and Re, the ratio of drag coefficients of slip-flow to the no-slip flow changes significantly by varying Kn. For flows without thermal creep effects [i.e., $(\partial T_s/\partial x) = 0.0$], the extra terms in the numerator of Eq. (17) are absent and the formula is further simplified.

To validate our computer code, which was developed for general complex geometries, we use the aforementioned analytical results. Comparisons are performed up to $Kn = 0.15$ and the results are presented in Fig. 1. The dashed line and the solid line show the drag reduction predicted by the first- and high-order slip-flow theory without thermal creep effects, respectively. The triangles correspond to numerical predictions with high-order slip-flow theory, and the circles correspond to numerical predictions with high-order slip-flow theory, including in this case the thermal creep effects [here $Ec = 1.0$, $Re = 1.0$ and $(\partial T_s/\partial x) = 1$]. The differences between the analytical and numerical results are negligible.

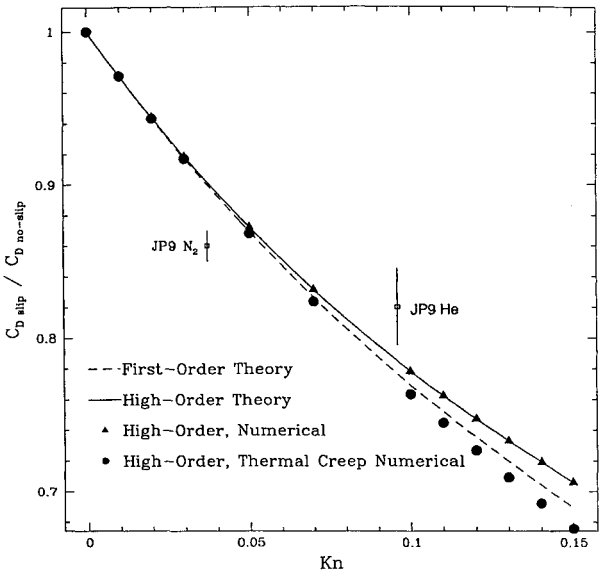

Fig. 1 Ratio of drag coefficients of slip-flow to no-slip flow in a pressure-driven channel. [Parameters for thermal creep results are $Ec = 1.0$, $Re = 1.0$ and $(\partial T_s/\partial x) = 1$.]

The aforementioned simplified analysis can also be used to explain the drag reduction obtained in the experiments reported in Ref. 14. Equation (17) is derived on the assumption of fully developed flow and is independent of Reynolds number for isothermal flow. The ratio predicted from Eq. (17) for $Kn = 0.044$ corresponding to the helium flow (case JP9 in Ref. 14) is 0.79 in good agreement with the measured value 0.8–0.85; the nitrogen flow gives a slightly greater pressure drop. These calculations assume an accommodation coefficient $\sigma_v = 1$; for smaller values of σ_v, achieved in practice, better agreement is obtained. In these comparisons we have assumed isothermal flow, and thus we have neglected the effect of thermal creep that may also contribute to higher drag reduction. For channel depths significantly smaller (corresponding to $Kn > 0.1$), the experimental results show a strong dependence of the ratio of drag coefficients on the Reynolds number not predicted by the above analysis.

Regarding heat exchange in microdomains, it is interesting to note that the viscous heating terms are quite significant. For example, if the reference temperature T_0 is taken to be the room temperature and the specified temperature difference of the domain ΔT is small, the viscous heating effects become non-negligible for $M \geq 0.05$ [see Eq. (13)]. An analytical solution of general heat convection problem for steady and thermally fully developed planar microchannel flows under specified heat flux $\dot{q}$ on the boundaries can be obtained by decomposing the temperature profile into two parts:

$$T(x, y) = \frac{\partial T_s}{\partial x}x + \theta(y) \tag{18}$$

where $(\partial T_s/\partial x)x$ and $\theta(y)$ shows the axial and crossflow temperature variations, respectively. The coordinates x and y are also nondimensionalized here with the reference length scale. A global energy balance in the domain with an insulated top surface and a specified constant heat flux on the bottom surface gives the following relation for the tangential temperature gradient along the channel:

$$\frac{\partial T_s}{\partial x} = \frac{1}{RePr\dot{Q}}\left(\dot{q} + \frac{8}{3}EcPr\right) \tag{19}$$

The corresponding crossflow temperature distribution in the channel is

$$\theta(y) = RePr\frac{\partial T_s}{\partial x}\left(B\frac{y^2}{2} - \frac{y^4}{12}\right) - EcPr\frac{y^4}{3} + Cy + D \quad (20)$$

where

$$B = 1 + 2\left(\frac{2-\sigma_v}{\sigma_v}\right)\frac{Kn}{1+\frac{1}{2}Kn} + \frac{3}{2\pi}\frac{(\gamma-1)}{\gamma}\frac{Kn^2Re}{Ec}\frac{\partial T_s}{\partial x} \quad (21)$$

$$C = RePr\frac{\partial T_s}{\partial x}\left(\frac{1}{3} - B\right) + \frac{4}{3}EcPr \quad (22)$$

$$D = \theta_0 - \frac{2\gamma}{\gamma+1}\frac{Kn}{Pr}\dot{q} + \frac{5}{3}EcPr - RePr\frac{\partial T_s}{\partial x}\left(\frac{3}{2}B - \frac{5}{2}\right) \quad (23)$$

where θ_0 is the reference temperature. The modifications to the coefficients B and D due to Kn shows the thermal creep, velocity slip, and temperature jump effects. The continuum solution is recovered as the rarefaction effects diminish (i.e., $Kn \to 0$).

A quadratic equation for $(\partial T_s/\partial x)$ can be obtained combining Eqs. (15) and (19). The solution for $(\partial T_s/\partial x)$ for specified heat fluxes is shown in Fig. 2 as a function of Mach number. Equation (13) is used to specify the Eckert number variation for both the continuum and the noncontinuum cases. The Knudsen number variations are specified by Eq. (12). It is seen that the heat flux required to maintain $(\partial T_s/\partial x) = 0$ is the same for both continuum and noncontinuum curves. The physical significance of this result is that for a specified Mach number there is only a single value of the heat flux required to compensate the viscous heating effects. Another significant result is the reduction in the magnitude of $(\partial T_s/\partial x)$ in noncontinuum flows, which implies that microchannels sustain smaller tangential temperature gradients compared to the large-scale channels. Examining Eq. (15) and Fig. 2, we see that the volumetric flow rate of a heated microchannel increases due to thermal creep effects. However, cooled microchannels allow less volumetric flow rate compared to the continuum case. If the rarefaction effects are increased further, the viscous heating effects will dominate. Under this condition $\partial T_s/\partial x$) may become positive, which will result in increase of the volumetric flow rate beyond the predictions of continuum theory even for cooled channels.

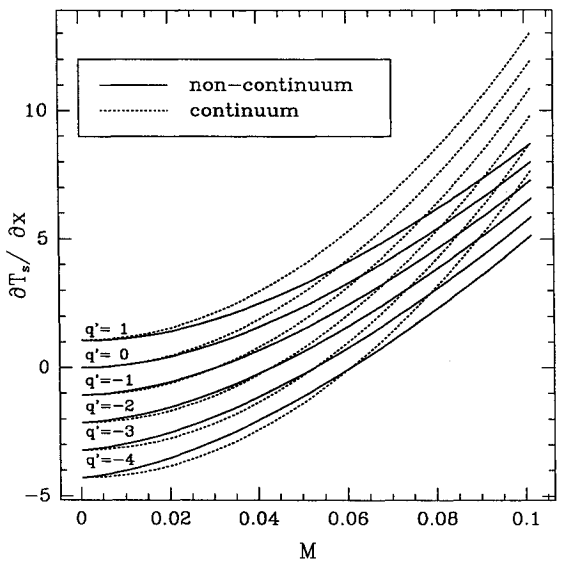

Fig. 2 Variation of tangential temperature gradient $(\partial T_s/\partial x)$ along the surface of a pressure-driven channel as a function of Mach number for different levels of heat fluxes $(\dot{q})$. (Re = 1.0, ΔT = 1 K and T_0 = 300 K).

The temperature jump diminishes if both surfaces of the channel are insulated (see Fig. 3, top row). In this case, the maximum temperature occurs near the walls where shear stresses are more dominant, and the tangential temperature variation becomes positive (see Fig. 2). This suggests significant changes in the volumetric flow rate of the microchannel, which is the main reason for the differences in the temperature profiles of two cases. Thermal creep in a microchannel can be avoided if the channel is carefully cooled with a cooling rate of $\dot{q} = -\frac{8}{3}PrEc$ [see Eq. (19)]; this results in constant temperature along the channel wall. The temperature distribution for a microchannel, without thermal creep effects, is also given in Fig. 3 (bottom row). It is seen that the temperature of the insulated surface is greater than its counterpart modeled by the continuum theory. The reason for this behavior is the temperature jump effects on the cooled surface of the channel.

The computational model developed here is based on the incompressibility approximation. In general, for Mach number values less than 0.2–0.3, flows can be approximated as incompressible. However, there are instances where the Mach number value and corresponding changes may be low, but the density and corresponding pressure variations may be large. For example, a severe case of compressibility effects is seen in the pressure-driven flows through long channels. In the experiments of Ref. 20 about an order of magnitude pressure drop is imposed through the microchannels, and thus strong compressibility effects are expected, although this was not documented in that work.

To investigate the conditions under which density variation in the channel is limited and thus the incompressibility assumption is still a valid one, we consider the following analysis. We approximate the pressure-driven channel flow as one-dimensional, adiabatic, constant area flow (i.e., Fanno flow). For our analysis we use the experimental data reported in Ref. 20. The Fanno flow equations can be derived by using a friction factor $[\bar{f} = (1/L)\int_0^L f\,dx]$ averaged along the channel of length L. The friction factor at any point in the channel can be evaluated as a function of local conditions denoted by x

$$f(x) = \frac{\tau_s(x)}{0.5\rho(x)U(x)^2} \quad (24)$$

where τ_s $[\tau_s = \mu(\partial U/\partial y)]$ is the shear stress on the wall. Since the mass flux (ρU) in the channel is constant, the friction factor can be assumed to be a function of dynamic viscosity $[\mu(T)]$ only [assuming $(\partial U/\partial y)/U$ is approximately a constant]. The dynamic viscosity variations are related to temperature via Sutherland's law, and thus the friction factor f essentially becomes a function of temparature. Therefore, for small temperature changes reported in the experiments of Ref. 20, the friction factor is approximately a constant along the streamwise direction.

The Mach number variation in the channel for Fanno flow can be obtained for specified friction factor as [see Ref. 21, Eq. (6.34)]:

$$\frac{dM^2}{dx} = \frac{\gamma M^4\{1 + [(\gamma-1)/2]M^2\}}{1 - M^2}\frac{4f}{D} \quad (25)$$

This equation integrated from inlet state (M_{in}) to any station x downstream of the channel results in

$$\frac{4\bar{f}x}{D} = \frac{\gamma+1}{2\gamma}\log_e\left(\frac{M_{in}^2\{1 + [(\gamma-1)/2]M^2\}}{M^2\{1 + [(\gamma-1)/2]M_{in}^2\}}\right) + \frac{(M^2 - M_{in}^2)}{\gamma M^2 M_{in}^2} \quad (26)$$

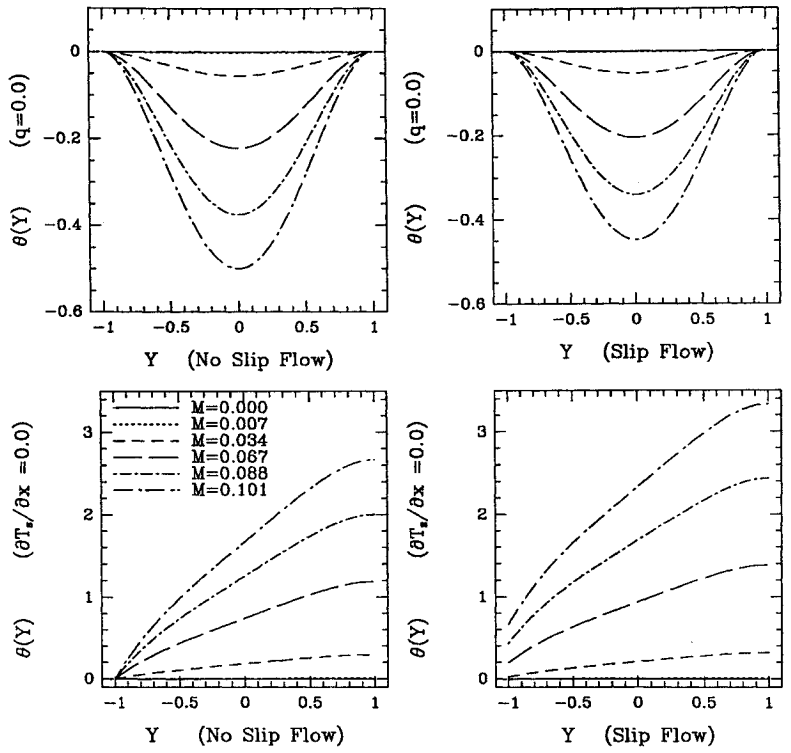

Fig. 3 Temperature profiles in a pressure-driven channel flow for continuum and noncontinuum flows as a function of Mach number. The top row shows insulated channel, and the bottom row shows channel with no thermal creep effects [i.e., $(\partial T_s/\partial x) = 0.0$]. $Re = 1.0$ and $Pr = 0.7$.

The variation of Mach number in the channel as a function of the inlet Mach number and $(4\bar{f}x/D)$ is found by plotting Eq. (26) for specified M_{in} and M values. Once the Mach number variation in the channel is known, the corresponding pressure ratio (P/P_{in}) and the density ratio (ρ/ρ_{in}) variations through the channel can be calculated by using the following relations:

$$\frac{P}{P_{in}} = \frac{M_{in}}{M}\left(\frac{\{1 + [(\gamma - 1)/2]M_{in}^2\}}{\{1 + [(\gamma - 1)/2]M^2\}}\right)^{1/2}$$
$$\frac{\rho}{\rho_{in}} = \frac{M_{in}}{M}\left(\frac{\{1 + [(\gamma - 1)/2]M^2\}}{\{1 + [(\gamma - 1)/2]M_{in}^2\}}\right)^{1/2} \quad (27)$$

The pressure ratio (P/P_{in}) variation in the channel as a function of $(4\bar{f}x/D)$ predicted by Fanno flow theory for specified inlet pressure of 8.0 atm and exit pressure of 1.0 atm, corresponding to case JP9 in Ref. 20, is presented in Fig. 4. It is seen that pressure ratio variation is almost linear for about 35–40% of the channel length, even for this large pressure ratio variation. This implies that the corresponding density ratio variation is also almost linear as the temperature is practically constant. Therefore, for smaller pressure ratio variations [approximately $(P_{out}/P_{in}) \geq 0.75$–$0.80$] the pressure drop and the density variations in the channel are approximately linear, and thus the incompressible results developed earlier can be applied by using the arithmetic average of the inlet and the exit Kn in the microchannel. Clearly, the compressibility effects in the experiments of Ref. 20 are so strong (because of specified large pressure drop) that rarefied gas effects are masked by the compressibility effects. This conclusion is further supported by the recent experimental findings of C. M. Ho and Y. C. Tai (work in progress). The analysis of a microchannel flow presented in Ref. 22 also considers the compressibility effects.

We consider next the flow between stationary parallel plates at the inlet of a microchannel as a prototype developing flow. A uniform velocity profile is specified at the inlet. In Ref. 11 the same case was calculated using a vorticity stream function formulation, and results were presented for different values

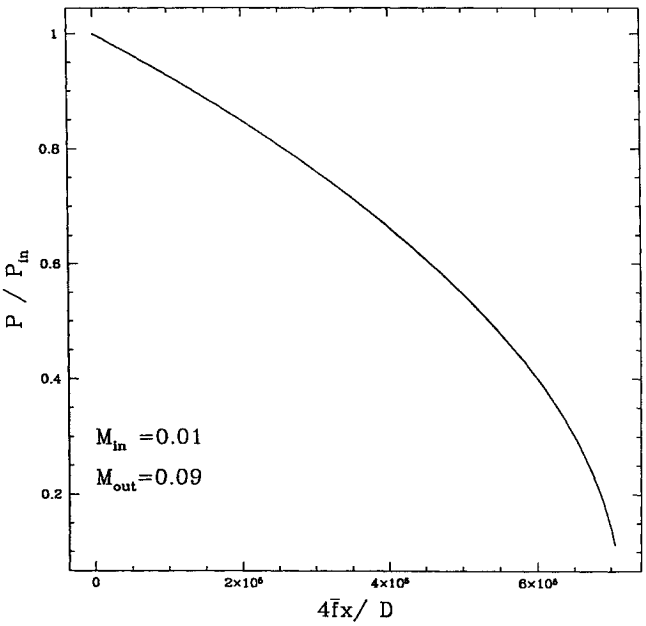

Fig. 4 Pressure ratio (P/P_{in}) variation through the channel as a function of $(4\bar{f}x/L)$. Inlet and the exit conditions corresponds to case JP9 in Ref. 19 ($P_{in} = 8.0$ atm, $P_{out} = 1.0$ atm; $M_{in} = 0.01$, $M_{out} = 0.09$).

of Reynolds and Knudsen number as well as accommodation coefficients. Here, we perform a simulation at $Re = 20$. In Fig. 5 we plot the slip velocity along the wall for $Kn = 0.03$, obtained by using both the first and high-order slip flow boundary conditions. It is seen that the slip effects are very dominant at the inlet of the channel and both results estimate the slip velocity to be about 50–60% of the incoming velocity U_∞. However, these effects are reduced well below 10% in the developed region of the flow. A relatively fine mesh was employed in the simulation consisting of $K = 40$ elements, each of 7×7 number of DOF. It is evident from the plot that the slip velocity experiences a very steep change from

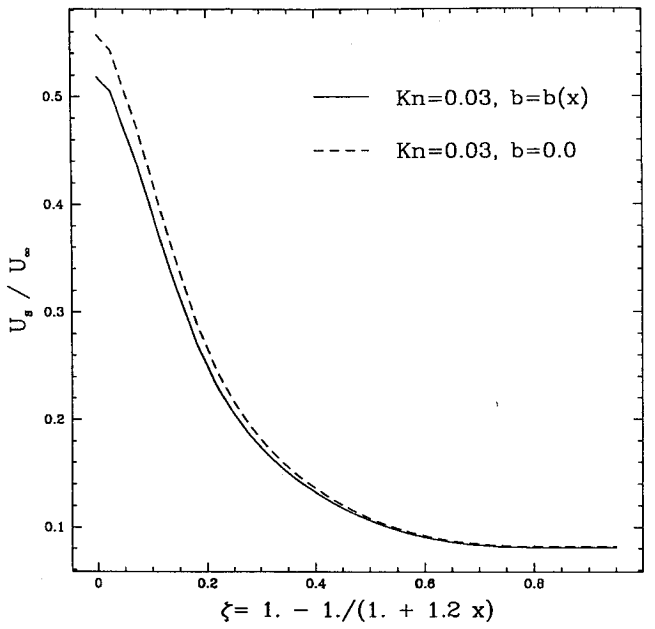

Fig. 5 Developing flow in microchannel; slip velocity along the wall $Kn = 0.03$. $Re = 20$. $X = (x/h)$.

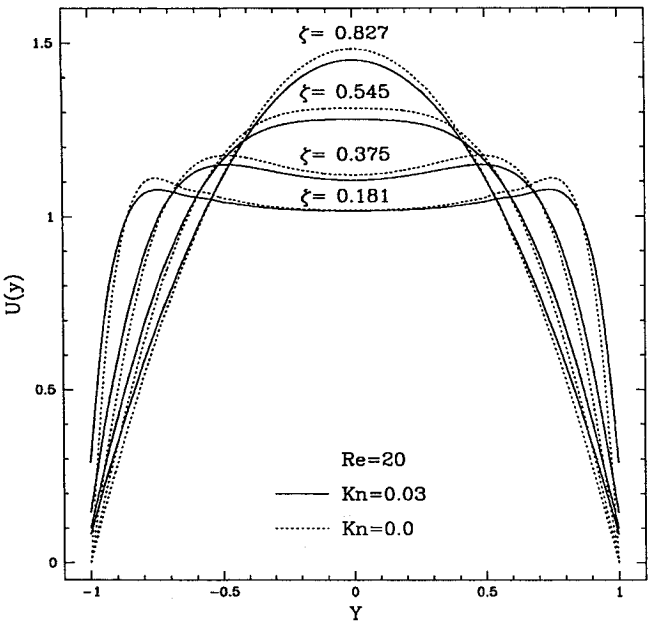

Fig. 6 Streamwise velocity profiles at various streamwise locations as a function of ζ [$Kn = 0.03$ (solid lines), and $Kn = 0.0$ (dashed lines, continuum case)].

the inlet to approximately a distance in the streamwise direction equal to the channel height, and achieves an asymptotic value corresponding to the fully developed profile approximately four channel heights downstream. The high-order slip effects reduce the slip velocity compared to the first-order predictions. In Fig. 6 we plot several streamwise velocity profiles close to inlet for $Kn = 0.03$ (solid line) and $Kn = 0$ (no-slip; dashed line). For various values of ζ close to the inlet ($\zeta \leq 0.75$), the maximum velocity is off centerline until a fully developed profile is established. We also see from the plot that the value of the maximum velocity is always smaller in the case of the slip-flow. This behavior of maximum velocities off the centerline cannot be obtained if the convective terms are linearized as in Ref. 23. Our results agree with the computations reported in Ref. 11, however, in that work the maximum values were underpredicted by more than a factor of 2 compared to our results. We verified the validity of our results by performing higher resolution (11 × 11) simulations.

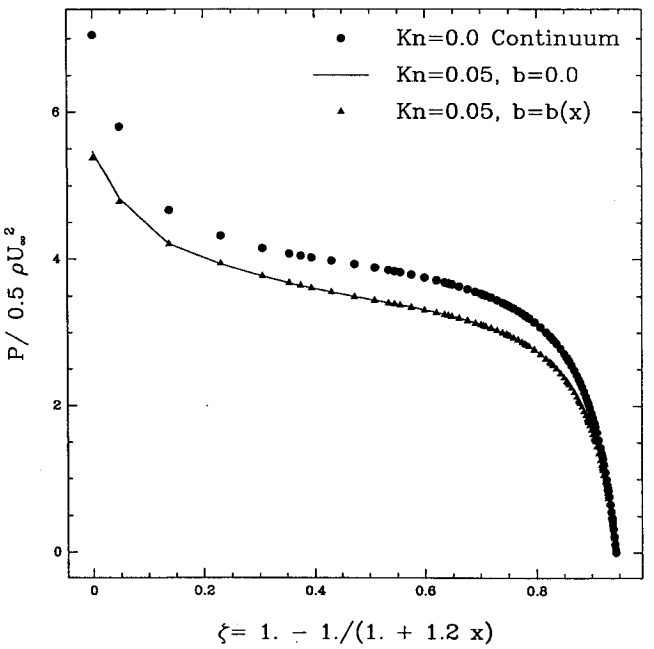

Fig. 7 Pressure distribution along the wall of the channel for slip-flow (using first-order, and high-order slip boundary conditions), and no-slip flow as a function of $X = (x/h)$.

This finding suggests that earlier computational results,[11,23] which underpredicted maxima, may have suffered from discretization errors. Finally, the static pressure distribution along the channel wall is plotted in Fig. 7. Due to the no-slip condition on the walls the continuum flow stagnates at the inlet of the channel, resulting in larger static pressure values than the corresponding slip-flow case. For both slip- and no-slip flows the pressure drops rapidly at the inlet until $\zeta \simeq 0.2$, then the pressure drop along the channel wall is parabolic until about $\zeta = 0.75[(x/h) = 2.5]$. Finally the pressure drop becomes linear for both slip and no-slip flows. The differences of pressure distribution between the linear and high-order slip flow simulations seems negligible in the scale of the plot, since the corresponding differences in slip velocity distribution of two cases are less than 5% of incoming velocity U_∞.

B. External Flows

In this section, a simulation of slip-flows past a circular cylinder is presented as a prototype of an external flow. Uniform flow past a cylinder with a slip surface has also been studied in Ref. 12 for attached flows using an approximate boundary-layer analysis. Here, we simulate both attached and separated flows ($Re = 1.0$ and $Re = 10.0$); the simulations are performed at two values of Knudsen number: $Kn = 0$ (no-slip) and $Kn = 0.015$. Separation of flow with a small circulation bubble is observed for $Re = 10$; the slip-flow direction is reversed inside the separation zone. In Fig. 8 we plot the magnitude of slip velocity distribution along the cylinder periphery for $Re = 1$ (attached flow; triangles) and $Re = 10$ (separated flow; circles); here, 0 deg corresponds to the front stagnation point. The slip velocity increases with the Reynolds number, but it decreases substantially in the separated (almost stagnant) region. This slip velocity is proportional to tangential stress τ_s that is plotted in Fig. 9 for the case of $Re = 10$. From this plot it is evident that separation occurs at an angle approximately 147 deg from the front stagnation point. For the range of Knudsen number ($0 < Kn < 0.015$) investigated in this paper no difference in the separation angle is observed. For comparison, we also plot the tangential stresses corresponding to the continuum case, $Kn = 0$. As expected, a reduction in skin friction is obtained especially in the front part of the cylinder where the flow accelerates.

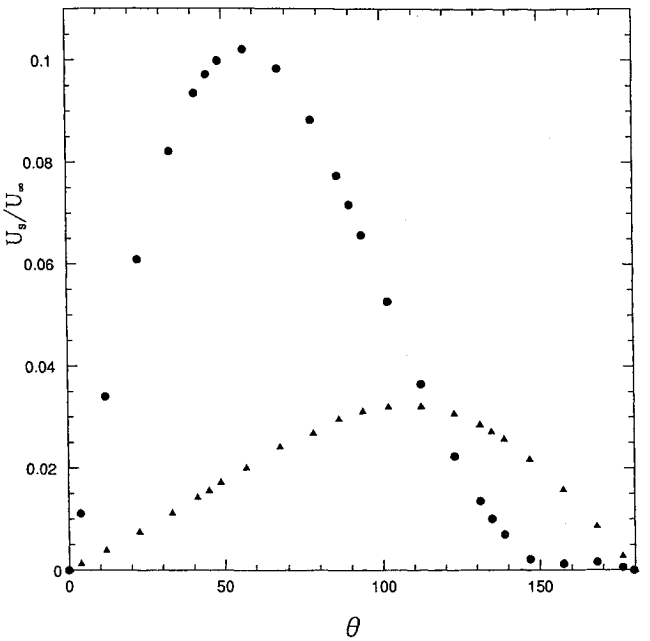

Fig. 8 The magnitude of slip velocity distribution along the periphery of a circular cylinder at Kn = 0.015, triangles, Re = 1; circles, Re = 10 (0 deg corresponds to the front stagnation point).

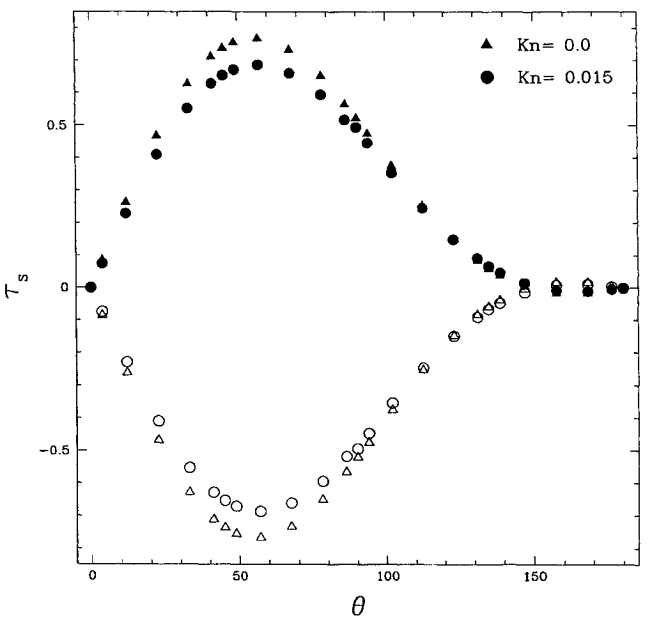

Fig. 9 Distribution of tangential stresses along the upper and lower surfaces of circular cylinder at Re = 10 and Kn = 0 (triangles, no-slip case), Kn = 0.015 (circles). Solid and blank symbols show upper and lower surfaces, respectively. Shear stresses are zero at about θ = 147 deg, where flow separates.

For incompressible flows over flat no-slip surfaces the viscous normal stress components τ_n are identically zero; however, in slip surfaces with curvature, the viscous normal stresses achieve finite values and increase substantially with the Knudsen number. This effect is demonstrated in Fig. 10 where we plot the viscous normal stress distribution around the cylinder periphery. In this case the viscous normal stresses for Kn = 0 are nonzero due to the curvilinear boundary; however, they are considerably smaller compared to the slip-flow, even for this relatively small value of Knudsen number (Kn = 0.015). Levels of the pressure distribution are also reduced compared to the no-slip case in agreement with the results of Ref. 12. The reduction in the pressure levels is counterbalanced by the increase in the viscous normal stresses; therefore, the total

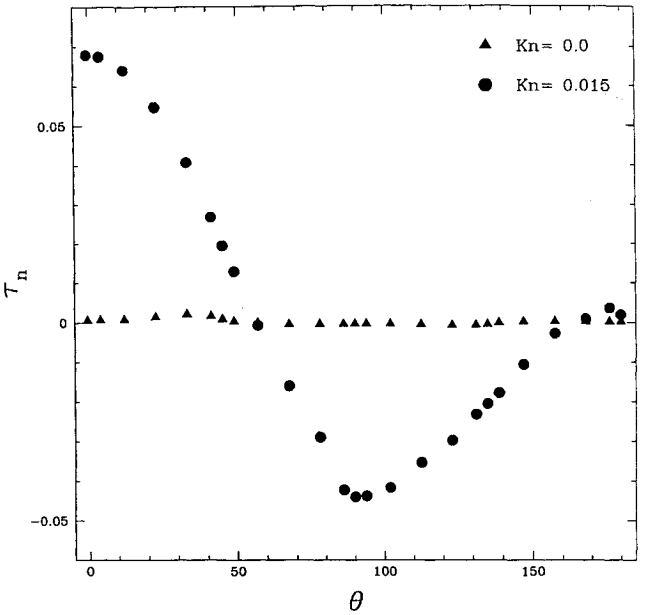

Fig. 10 Distribution of viscous normal stresses along the cylinder periphery at Re = 10 and Kn = 0 (triangles, no-slip case), Kn = 0.015 (circles).

normal stresses (i.e., combined pressure and viscous normal stresses) does not vanish as the rarefaction effects increase.[12]

IV. Discussion

We have developed a numerical model to simulate unsteady two- and three-dimensional flows in complex microdomains. The current methodology is valid for slip-flow regime (i.e., for values of Knudsen number less than approximately 0.1). For higher values of Knudsen number, direct solution of the Boltzmann equation is required, although the simplified model developed in Ref. 6, which still employs conservation laws, can potentially be used in the context of microtransport modeling. Drag reduction phenomena apparent in microchannels can be explained by the slip-flow theory. However, the coupling of momentum and energy transport via thermal creep and viscous heating effects can make the analysis of the problem quite difficult. The high-order slip boundary conditions introduced by the expansion parameter b and the significance of high-order slip effects, especially for separated flows, are still under investigation. It is clear, for instance, that the aforementioned analysis is invalid in the neigborhood of a separation point. Another important issue we are currently investigating is the effect of compressibility. The Fanno flow approximation discussed here, and in more detail in Ref. 15, suggests that for severe pressure drops compressibility effects dominate, and thus the influence of rarefied gases on the skin friction distribution is secondary. This conclusion is also supported by recent experimental data (C. M. Ho and Y. C. Tai, work in progress). The spectral element method has recently been extended to compressible Navier-Stokes equations.[15] Simulation results for a detailed quantification of compressibility effects, as well as more extensive comparisons with the experimental results of Ho and Tai (currently unpublished), will be presented in a future publication. Finally, the methodology we have developed is general and can be applied to simulations of three-dimensional flows in existing microdevices such as lifting microblades, microbearings, and micromotors.[15]

Acknowledgments

This work was supported by NSF Grant ECS-90-23760 under the supervision of George Lea. We are grateful to the reviewers for their insightful comments and the useful references they suggested to us. We would also like to thank D.

Cho and W. Trimmer for many useful discussions, and S. H. Lam for his suggestions regarding the high-order boundary condition.

References

[1]Gabriel, K., Javris, J., and Trimmer, W., "Small Machines, Large Opportunities," National Science Foundation Rept. 1988.

[2]O'Connor, L., "MEMS: Microelectromechanical Systems," *Mechanical Engineering Journal*, Vol. 114, No. 2, 1992, pp. 40–47.

[3]Eringen, A. C., "Simple Microfluids," *International Journal of Engineering and Science*, Vol. 2, No. 2, 1964, pp. 205–217.

[4]Chapman, S., and Cowling, T. G., *The Mathematical Theory of Non-Uniform Gases*, Cambridge Univ. Press, Cambridge, England, UK, 1970.

[5]Schaaf, S. A., and Chambre, P. L., *Flow of Rarefied Gases*, Princeton Univ. Press, Princeton, NJ, 1966.

[6]Shen, S. F., "A Simplified Description of Rarefied-Gas Flows by Means of the Hydrodynamic Equations," *Fundamental Phenomena in Hypersonic Flow*, Cornell Univ. Press, New York, 1966, pp. 239–258.

[7]Seidl, M., and Steinheil, E., "Measurement of Momentum Accommodation Coefficients on Surfaces Characterized by Auger Spectroscopy, SIMS and LEED," *Proceedings of the 9th International Symposium on Rarefied Gas Dynamics*, DFVLR-Press, Göttingen, Germany, 1974, pp. E9.1–E9.2.

[8]Lord, R. G., "Tangential Momentum Coefficients of Rare Gases on Polycrystalline Surfaces," *Proceedings of the 10th International Symposium on Rarefied Gas Dynamics* (Aspen, CO), AIAA, New York, 1976, pp. 531–538.

[9]Patera, A. T., "A Spectral Element Method for Fluid Dynamics; Laminar Flow in a Channel Expansion," *Journal of Computational Physics*, Vol. 54, No. 3, 1984, pp. 468–488.

[10]Karniadakis, G. E., "Spectral Element Simulations of Laminar and Turbulent Flows in Complex Geometries," *Applied Numerical Mathematics*, Vol. 6, 1989, pp. 85–105.

[11]Gampert, B., "Inlet Flow with Slip," *Proceedings of the 10th International Symposium on Rarefied Gas Dynamics* (Aspen, CO), AIAA, New York, 1976, pp. 225–235.

[12]Gampert, B., "Low Reynolds Number TAC-Slip Flow Past a Circular Cylinder," *Proceedings of the 11th International Symposium on Rarefied Gas Dynamics*, CEA, Cannes, France, 1978, pp. 255–267.

[13]Gampert, B., "Velocity-Slip and Temperature-Jump Effects in Similar, Slightly Rarefied Laminar Boundary-Layer Flow Past Surfaces with Incomplete Momentum and Energy Accommodation," *Proceedings of the 12th International Symposium on Rarefied Gas Dynamics*, AIAA, New York, 1980, pp. 1105–1121.

[14]Pfahler, J., Harley, J., Bau, H., and Zemel, J., "Gas and Liquid Flow in Small Channels," *American Society of Mechanical Engineers Journal*, Vol. 32, 1991, pp. 49–59.

[15]Beskok, A., "Simulation of Heat and Momentum Transfer in Complex Micro-Geometries," M.S. Thesis, Princeton Univ., Mechanical and Aerospace Engineering Dept., Princeton, NJ, June 1994.

[16]Zhong, X., "On Numerical Solutions of Burnett Equations for Hypersonic Flow Past 2-D Circular Blunt Leading Edges in Continuum Transition Regime," AIAA Paper 93-3092, 1993.

[17]Hsia, Y. T., and Domoto, G. A., "An Experimental Investigation of Molecular Rarefaction Effects in Gas Lubricated Bearings at Ultra-Low Clearances," *Transactions of the American Society of Mechanical Engineers*, Vol. 105, 1983, pp. 120–130.

[18]Karniadakis, G. E., Israeli, M., and Orszag, S. A., "High-Order Splitting Methods for the Incompressible Navier-Stokes Equations," *Journal of Computational Physics*, Vol. 97, No. 9, 1989, pp. 414–443.

[19]Kennard, E. H., *Kinetic Theory of Gases*, McGraw-Hill, New York, 1938.

[20]Harley, C. J., "Compressible Gas Flow in Micron and Submicron Sized Channels," M.S. Thesis, Univ. of Pennsylvania, Philadelphia, PA, 1991.

[21]Thompson, A. P., *Compressible Fluid Dynamics*, Advanced Engineering Series, Rensselaer Polytechnic Inst., Troy, NY, 1988, p. 299.

[22]Arkilic, E., and Breuer, K. S., "Gaseous Flow in Small Channels" AIAA Paper 93-327, July 1993.

[23]Sparrow, E. M., Lundgren, T. S., and Lin, S. H., "Slip Flow in the Entrance Region of a Parallel Channel," *Proceedings of the Heat Transfer and Fluid Mechanics Institute*, Stanford Univ. Press, Stanford, CA, 1962, pp. 223–238.